Mon. Not. R. Astron. Soc. **382,** 543–552 (2007) doi:10.1111/j.1365-2966.2007.12466.x

An Australia Telescope Compact Array 20-cm radio continuum study of the Large Magellanic Cloud

A. Hughes,[1,2]★ L. Staveley-Smith,[3] S. Kim,[4] M. Wolleben[5,6] and M. Filipović[7]

[1]*Centre for Supercomputing and Astrophysics, Swinburne University of Technology, Hawthorn VIC 3122, Australia*
[2]*CSIRO Australia Telescope National Facility, PO Box 76, Epping NSW 1710, Australia*
[3]*School of Physics M013, University of Western Australia, Crawley WA 6009, Australia*
[4]*Department of Astronomy and Space Science, Sejong University, KwangJin-gu, KunJa-dong 98, Seoul 143-747, Korea*
[5]*Department of Electrical and Computer Engineering, University of Alberta, Edmonton AB T6G 2V4, Canada*
[6]*National Research Council Canada, Herzberg Insitute of Astrophysics, Dominion Radio Astrophysical Observatory, Penticton BV V2A 6J9, Canada*
[7]*University of Western Sydney, Locked Bag 1797, Penrith South, DC, NSW 1797, Australia*

Accepted 2007 September 12. Received 2007 September 5

ABSTRACT

We present a mosaic image of the 1.4-GHz radio continuum emission from the Large Magellanic Cloud (LMC) observed with the Australia Telescope Compact Array (ATCA) and the Parkes Telescope. The mosaic covers $10.^{\circ}8 \times 12.^{\circ}3$ with an angular resolution of 40 arcsec, corresponding to a spatial scale of ∼10 pc in the LMC. The final image is suitable for studying emission on all scales between 40 arcsec and the surveyed area. In this paper, we discuss (i) the characteristics of the LMC's diffuse and compact radio continuum emission, (ii) the fraction of the emission produced by thermal processes and the implied star formation rate in the LMC and (iii) variations in the radio spectral index across the LMC. Two non-standard reduction techniques that we used to process the ATCA visibility data may be of interest for future wide-field radio continuum surveys. The data are open to the astronomical community and should be a rich resource for studies of individual objects such as supernova remnants, H II regions and planetary nebulae as well as extended features such as the diffuse emission from synchrotron radiation.

Key words: techniques: interferometric – galaxies: individual: Large Magellanic Cloud – galaxies: ISM – Magellanic Clouds – radio continuum: galaxies.

1 INTRODUCTION

Radio continuum emission is a useful tool for studying star formation processes in galaxies. The two main components of the emission are thermal free–free radiation from ionized gas in H II regions and synchtron radiation emitted by relativistic electrons accelerated in magnetic fields (Condon 1992). Both processes are thought to be related to the evolution of massive stars, but they provide information about different periods in the galaxy's star formation history. Thermal radio emission arises directly from the ionized gas surrounding young massive stars. The intensity of the emission is proportional to the total number of Lyman continuum photons, and in the optically thin regime, the spectrum is nearly flat ($\alpha = -0.1$, where we adopt the convention $S_\nu \propto \nu^\alpha$). For an isolated star-forming region, the thermal radio emission should persist over time-scales similar to the average lifetime of an H II region (∼10 Myr), suggesting that the thermal component of a galaxy's radio continuum emission should be a good tracer of the current star formation rate (SFR) (e.g. Kennicutt 1998). The non-thermal emission, on the other hand, originates in the supernova explosions and supernova remnants (SNRs) that occur at the end of a massive star's life. If discrete SNRs were solely responsible for accelerating the relativistic electrons that emit synchrotron radiation, then the time-scale of the non-thermal radio emission would also be relatively short and the emission would provide another tracer of the galaxy's current star formation activity. However, observations of normal spiral galaxies suggest that only ∼10 per cent of a galaxy's synchrotron emission is due to electrons accelerated in the magnetic field of discrete SNRs; the remainder is from electrons accelerated in the widespread galactic field over time-scales of 10 to 100 Myr (Helou & Bicay 1993). For a galaxy with a single isolated star-forming region, the emission from discrete SNRs might still be expected to dominate the non-thermal component at early times (before the relativistic electrons have had time to diffuse away from their production sites), while very young starbursts (⩽3 Myr) should show almost no synchrotron radiation since the massive stars have not yet evolved into supernovae. These general considerations about the time-scales of the thermal and non-thermal radio continuum emission have prompted several groups to explore whether the radio spectral index might prove to be a useful

★Email: ahughes@astro.swin.edu.au

method to chronicle the star formation activity of starburst activity in simple systems (e.g Bressan, Silva & Granato 2002; Cannon & Skillman 2004; Hirashita & Hunt 2006).

In this paper, we present a new, high-resolution survey of the 1.4-GHz radio continuum emission from the Large Magellanic Cloud (LMC). The LMC is a gas-rich, irregular dwarf galaxy that exhibits clear signs of active star formation. Reddening and extinction due to dust in the LMC are low ($E_{B-V} \sim 0.13$, Massey et al. 1995), and the LMC's declination is such that our view of the galaxy is mostly uncontaminated by foreground emission from the Milky Way. The inclination of the LMC is also reasonably slight ($i \sim 35^\circ$, van der Marel & Cioni 2001), minimizing line-of-sight confusion. The LMC thus presents a unique opportunity to study an entire galaxy at high angular resolution. At an assumed distance of 50.1 kpc (Alves 2004), 1 arcmin corresponds to 15 pc, making the LMC an excellent laboratory to investigate the relationship between different phases of the interstellar medium (ISM), the interaction of the ISM with individual objects and the influence of galactic-scale processes on the properties of interstellar material. Recently completed surveys such as the Magellanic Cloud Emission Line Survey (MCELS, Smith & MCELS Team 1998), the Australia Telescope Compact Array (ATCA)+Parkes H I 21-cm survey (Kim et al. 1998, 2003), the *Spitzer* surveying the Agents of a Galaxyś Evolution project in the far-infrared (FIR) (Meixner et al. 2006) and the ^{12}CO ($J = 1 \rightarrow 0$) survey by NANTEN (Fukui et al. 2001) have the potential to provide a comprehensive view of the dust and gas phases in the LMC's interstellar medium, along with a complete inventory of stars and protostars. A high angular resolution survey of the radio continuum emission in the LMC is a timely and important complement to these data sets. In addition to the total intensity images that we present here, new studies of the polarization and Faraday rotation of background sources in the ATCA+Parkes radio continuum data have begun to reveal the strength and detailed structure of the LMC's magnetic field (Gaensler et al. 2005a,b).

This paper is organized as follows. In Section 2, we present the observing strategy of our survey. The methods that we used to reduce and combine the interferometer and single-dish data are described in Section 3. In Section 4, we present the final 1.4-GHz image of the LMC and examine spatial variations in the LMC's radio spectral index. We estimate the thermal fraction of the radio continuum emission and compare the radio-derived SFR for the LMC to estimates determined via other SFR calibrations. Section 5 contains a summary of our conclusions and outlines some potential future uses for the radio continuum data.

2 OBSERVATIONS

These observations of the LMC were conducted at the ATCA at the time of the H I survey by Kim et al. (1998, 2003) in a second frequency chain centred on 1384 MHz. The ATCA is an east–west interferometer located at the Paul Wild Observatory in Narrabri, Australia. The latitude of the ATCA is $-30^\circ 18$ arcmin. The interferometer consists of five 22-m antennae positioned along a 3 km track, with a sixth antenna located 3 km from the western end of the track. Observations of the LMC were made with four 750-m arrays between 1994 October and 1996 February. The observing log is presented in Table 1. Across the four array configurations, there are a total of 40 independent baselines ranging from 30 to 750 m. The ATCA antenna stations are regularly spaced, with the consequence that all possible baselines are incremented by multiples of 15.3 m.

For our survey, we mapped a $10.^\circ 8 \times 12.^\circ 3$ field covering the LMC, centred on $(05^{\rm h}20^{\rm m}, -68^{\rm d}44^{\rm m})_{\rm J2000}$. We divided the total survey area into 12 regions, each containing 112 pointing centres. The array was cycled around the 112 pointing centres within each region according to a hexagonal grid pattern determined by Nyquist's theorem. In this case, the angular separation of the pointing centres is given by

$$\theta = \frac{2}{\sqrt{3}} \frac{\lambda}{2D}, \quad (1)$$

where λ is observing wavelength and D is the diameter of the antenna. For our observations, $\lambda = 21$ cm and $D = 22$ m, giving a pointing centre separation of $\theta = 19$ arcmin. Each pointing was observed between 95 and 140 times during the entire survey, which corresponds to between 18 and 26 min of total integration time per pointing. A map of the pointing centres and scanning direction for the ATCA mosaic is shown in Fig. 1. The $u - v$ coverage for a single pointing centre within the mosaic is shown in Fig. 2.

All our observations were recorded in wide-band continuum mode with 32 4-MHz channels across a total bandwidth of 128 MHz. The centre frequency was 1.384 GHz. The ATCA feeds receive two orthogonal linear polarizations, X and Y. For the continuum observations, we measured the four polarization products XX, YY, XY and YX. Here, we only discuss the total intensity data; a preliminary analysis of the polarized emission has already been presented by Gaensler et al. (2005a). The H I emission from neutral hydrogen in the LMC was recorded simultaneously in the second frequency chain. The processing and analysis of the H I data have been described elsewhere (Kim et al. 1998, 2003).

Table 1. Summary of observing dates and array configuration.

Date	Array configuration
1994 October 26–November 9	750D
1995 February 23–March 11	750A
1995 June 02–June 07	750B
1995 October 15–October 31	750B
1996 January 27–February 8	750C

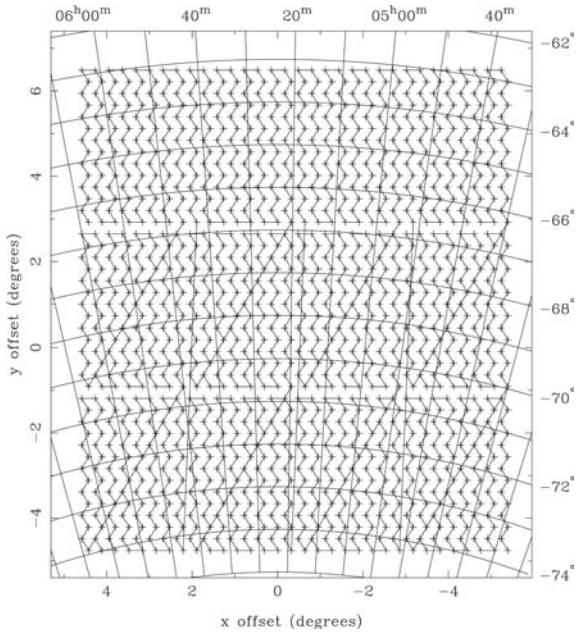

Figure 1. The scanning strategy and individual pointing centres of the ATCA LMC mosaic.

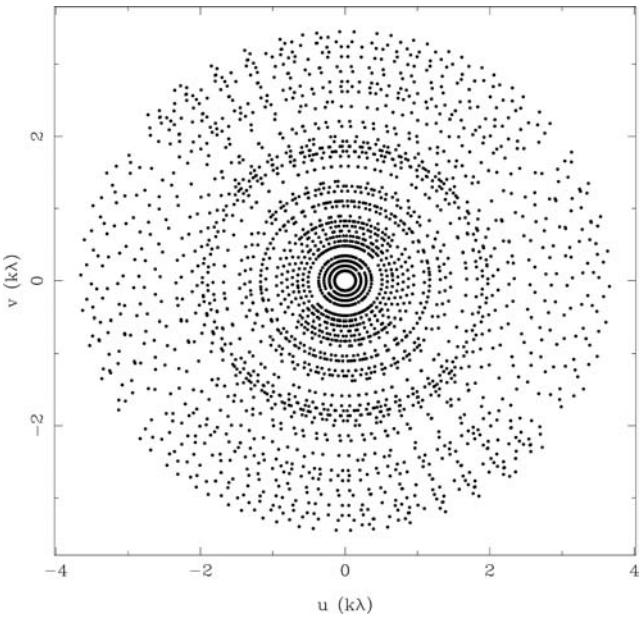

Figure 2. $u - v$ coverage of a single pointing within the ATCA LMC mosaic.

Previous studies that have made use of the radio continuum data that we present here include Cohen, Staveley-Smith & Green (2003) and Hughes et al. (2006). The data used in these publications were processed according to the procedure outlined in Section 3 except that the peeling technique (described in Section 3.2) was not applied.

3 DATA REDUCTION

The ATCA data were flagged, calibrated and imaged using the MIRIAD software package (Sault, Teuben & Wright 1995). We used the source PKS B1934−638 for bandpass and absolute flux density calibration (the flux density of PKS B1934−638 at 1.377 GHz is 14.95 Jy). One of either PKS B0407−658 or PKS B0454−810 was observed every 30 min in order to calibrate the time variation in the complex antenna gains. PKS B1934−638 has no detectable linear polarization and can thus be used to solve for polarization leakages. We had sufficient parallactic angle coverage of the two secondary calibrators to disentangle their intrinsic and instrumental polarization, allowing us to calibrate Stokes U and Q as well as total intensity.

The individual pointings were linearly combined and imaged using a standard grid-and-FFT scheme with superuniform weighting. Like uniform weighting, superuniform weighting minimizes sidelobe levels to improve the dynamic range and sensitivity to extended structure of the final mosaicked image. Uniform weighting reduces to natural weighting, however, if the total field of view of the mosaic is much larger than the primary beam. Superuniform weighting overcomes this limitation by decoupling the weighting from the size of the field. It attempts to minimize sidelobe contributions from strong sources over a region smaller than the total image and is typically more successful than uniform weighting for large mosaics (Sault, Staveley-Smith & Brouw 1996).

3.1 Image Deconvolution

We developed a two-step Fourier deconvolution strategy for our LMC data. After inverting the mosaic visibilities, we constructed a preliminary CLEAN model of our data by using 1.2 million iterations of the Steer-Dewdney-Ito (SDI) CLEAN algorithm on our dirty map (Steer, Dewdney & Ito 1984). The residuals of the CLEAN model, mainly corresponding to diffuse emission, were deconvolved using maximum entropy. The CLEAN model and the maximum entropy model were linearly combined and restored with a 40-arcsec Gaussian beam in order to form the final image.

3.2 Peeling

The deconvolved ATCA image exhibits ring-like artefacts at the ∼0.5 per cent level. These become significant close to bright compact sources such as 30 Doradus, limiting the sensitivity that can be achieved in these regions. These artefacts are mainly due to errors in the calibration of off-axis sources. There are number of possible causes for off-axis calibration errors, including pointing errors, small differences between individual antenna dishes, errors in the primary beam model and the rotation of the primary beam diffraction lobes through off-axis sources. In order to improve the dynamic range of the ATCA image, we applied a "peeling" technique that has been described by Tom Oosterloo (private communication). Contrary to the usual assumption that one set of antenna gain solutions is adequate across the field of a single pointing, peeling explicitly solves for the antenna gains at the position of off-axis sources, so that different calibration solutions can be applied to different regions within the field of each pointing.

In order to determine which pointings were badly affected by errors from off-axis sources, we deconvolved and imaged the visibility data for each of the 1344 pointings. Peeling was attempted if the following criteria were satisfied: (i) the flux density of the off-axis source was greater than 10 mJy beam^{-1}, (ii) the off-axis source was located more than 1.5 times the primary beam full width at half-maximum (FWHM) from the pointing centre and (iii) errors due to the off-axis source were evident within the primary beam. If these criteria were not satisfied, no corrections to the visibility data were made. If off-axis errors were deemed significant, we constructed a simple model of the on-axis sources using 10 000 iterations of the SDI CLEAN algorithm and subtracted the model of the on-axis sources from the visibility data. The resulting visibility data (the "model data") represent the off-axis source and its associated errors. The model data were imaged, and a model of the off-axis source was constructed using 10 000 iterations of the SDI CLEAN algorithm. We then performed an amplitude and phase self-calibration on the model data in order to obtain a good set of antenna gain solutions for the off-axis source (the "model gains"). The model gains were applied to the original visibility data for the pointing, and then the model of the off-axis source was subtracted. Next, the model gains were "un-applied" to the model-subtracted visibility data, that is, having multiplied the original visibility data by the antenna gain solutions for the off-axis source, we multiplied the model-subtracted visibility data by the inverse of these model gains. At the end of this process, we are left with visibility data that are identical to the original visibility data for the pointing, except that the off-axis source and its errors have been removed. As an example, Fig. 3 illustrates the main stages of the peeling process for a single pointing in the ATCA mosaic.

For a number of pointings, additional corrections to the basic antenna gain solutions were required due to calibration errors for sources located within the primary beam. To improve the antenna gain solutions for these pointings, amplitude and phase self-calibration were applied. In total, the peeling technique was applied to 269 of the 1344 pointings. On-axis self-calibration was applied to a further 78 pointings. The final set of corrected visibility data

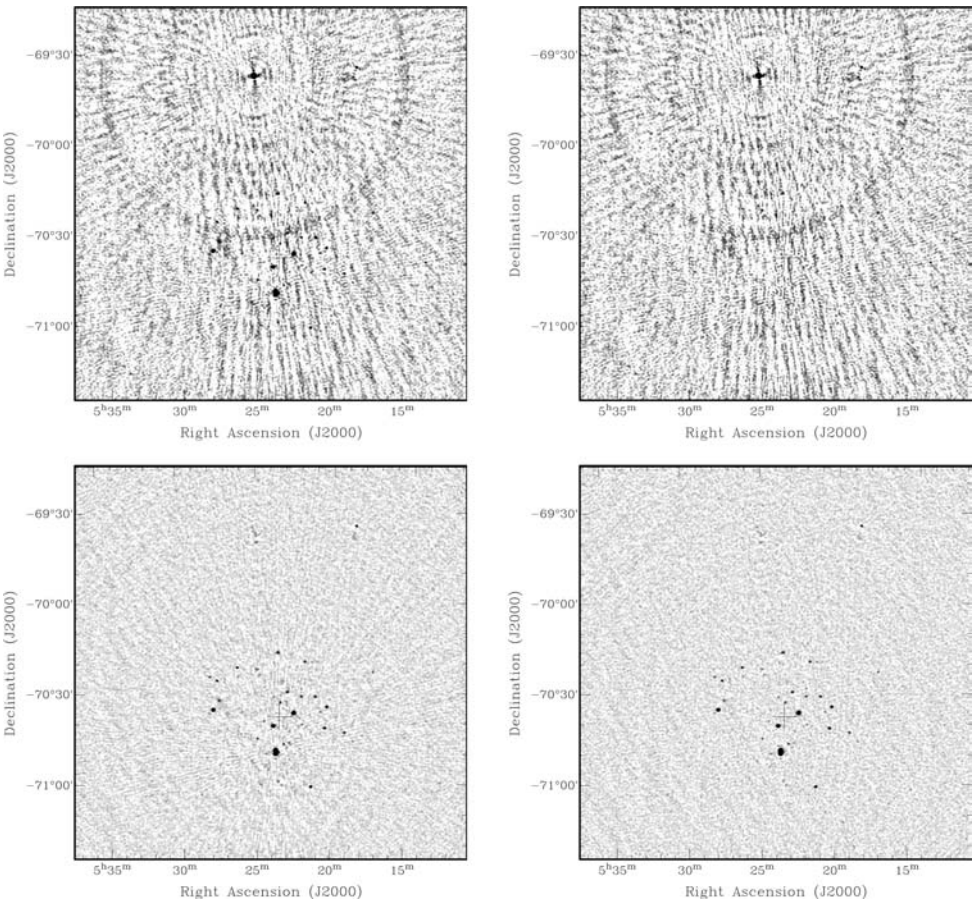

Figure 3. Example of peeling procedure for a single pointing of the ATCA mosaic. Only the region of sky containing the field centre and off-axis source is shown. The field centre is indicated with a black cross. Top left-hand panel: original image of the pointing. Top right-hand panel: image of the pointing after the on-axis sources have been subtracted. The appropriate gain solution for the off-axis source is then determined from this data using self-calibration. Bottom left-hand panel: image of the pointing after subtracting the off-axis source and its associated errors. Bottom right-hand panel: final image of the pointing after performing self-calibration on the on-axis sources.

were combined, deconvolved, imaged according to the strategy described in Section 3.1 above. The final ATCA-only mosaic is shown in Fig. 4. To highlight the improvement achieved by applying the peeling process, we present a expanded view of the 30 Doradus region in Fig. 5.

3.3 Combination of Inteferometer and Single-Dish Data

Although mosaicing recovers angular scales larger than normal interferometric observations by reducing the effective shortest projected baseline, our observations are still limited to angular scales smaller than $\theta = \lambda/(d–D/2)$, where $d = 30.6$ m is the shortest baseline of the ATCA and $D = 22$ m is the diameter of a single antenna. In our case, the ATCA data are limited to angular scales smaller than ∼34 arcmin. To recover information on larger scales, the ATCA mosaic data were combined with single-dish data from the Parkes Telescope. Here, we only provide information about the Parkes data that is relevant for the combination process; a detailed description of the single-dish observations and data reduction was presented in Haynes et al. (1986).

Single-dish and interferometer data may be combined in the Fourier domain after deconvolution of the individual pointings or in the $u - v$ plane prior to deconvolution. Stanimirovic (2002) showed that comparable results are achieved using either method but combining the data after deconvolution typically produced

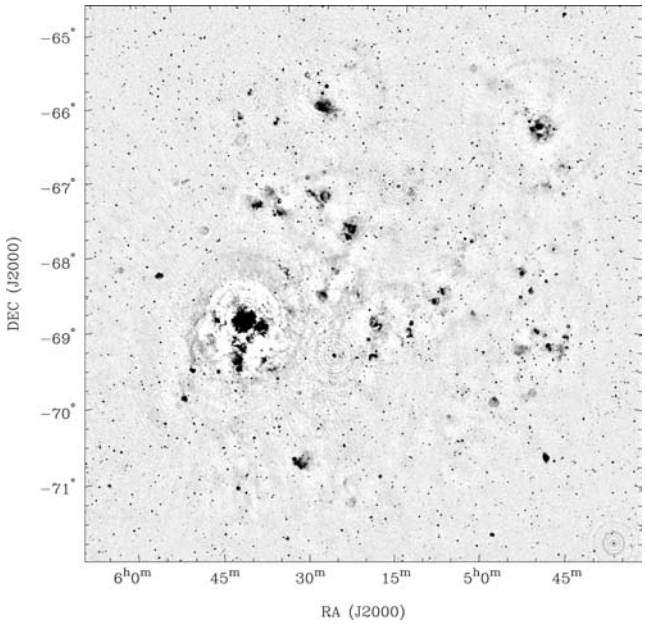

Figure 4. The deconvolved ATCA 1.4-GHz mosaic, after peeling and self-calibration of individual pointings but prior to combination with the single-dish data.

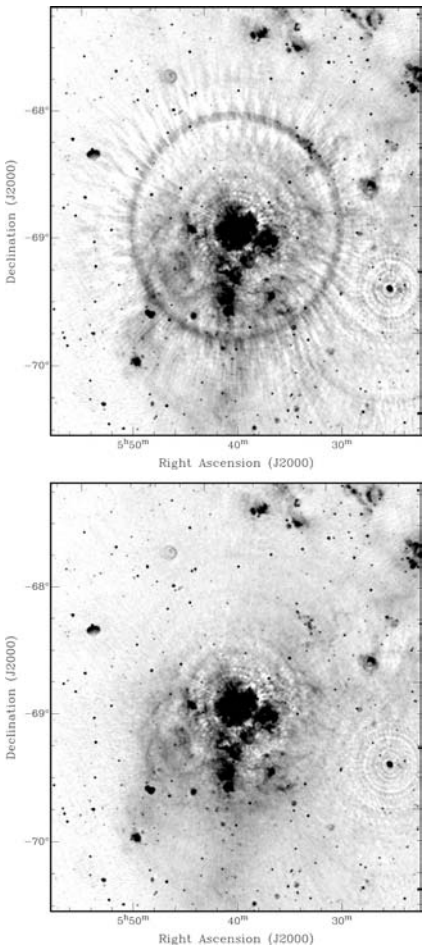

Figure 5. 1.4-GHz emission in the 30 Doradus region of the LMC. The two panels illustrate the final ATCA+Parkes image of this region with (bottom panel) and without (top panel) applying peeling corrections to the visibility data.

results that were more consistent with other methods. We chose to combine the data in the Fourier plane after deconvolution. In this method, the ATCA continuum data are imaged and deconvolved, the single-dish data are imaged, and the CLEAN interferometric and single-dish images are then Fourier transformed and combined. The method is implemented in the MIRIAD task IMMERGE.

Slight differences in calibration of the interferometer and single-dish data can necessitate a relative flux correction factor. This correction factor is determined by comparing the data sets in the Fourier plane at every pixel and frequency in the range of overlapping spatial frequencies. To calculate the calibration factor, both images must be deconvolved, a step which requires a good knowledge of the single-dish beam. Using a two-dimensional Gaussian with FWHM = 16.6 arcmin for the Parkes beam and by comparing the flux densities of strong, compact sources in the Parkes and ATCA data, we calculated a relative calibration factor of 1.07. The final ATCA+Parkes combined image is shown in Fig. 6.

3.4 Characteristics of the Final Image

The final combined image shown in Fig. 6 is sensitive to all angular scales from the synthesized beam size (40 arcsec) up to the final image size. In order to estimate the map sensitivity, we measured the average rms of blank regions of sky, finding 0.3 mJy per

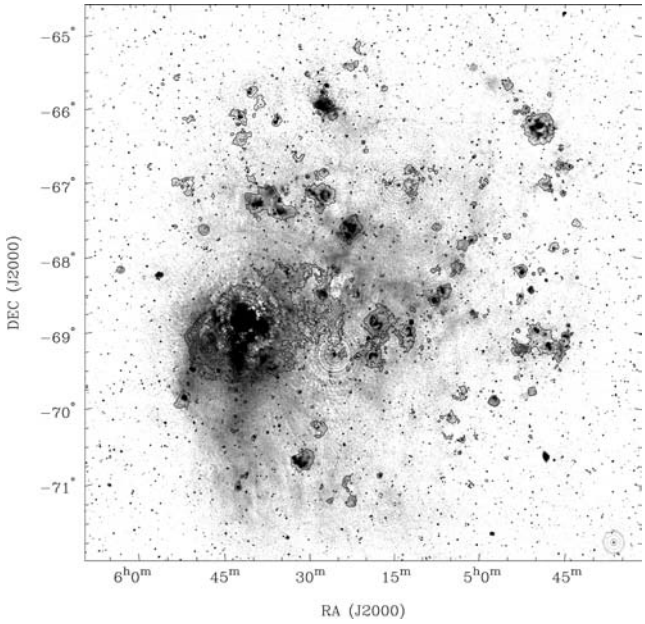

Figure 6. The final combined Parkes + ATCA 1.4-GHz radio continuum map of the LMC. A square-root intensity scale has been used to emphasize the characteristics of the diffuse emission. The black contours indicate an Hα brightness of 50 R (compare Fig. 8).

40-arcsec beam for the ATCA data, 30 mJy per 16.6-arcmin beam for the Parkes data and 0.3 mJy per 40-arcsec beam for the combined data. The measured value for the sensitivity of the ATCA data is in excellent agreement with the theoretical noise estimate of 0.3 mJy per 40-arcsec beam for our selected observing strategy and deconvolution scheme. Measuring the sensitivity of the ATCA and ATCA+Parkes data is somewhat complicated by the large number of point sources in the sky at 1.4 GHz, limiting the size of blank regions where a noise estimate can be reliably measured. To verify our sensitivity estimate, we produced a median-filtered version of the ATCA+Parkes image. The filtering operation, implemented in the GIPSY routine MFILTER, moves a $2.5 \times 2.5\,\mathrm{arcmin}^2$ window across the map, replacing the central pixel value (S_{cpix}) with the median value of the window (S_{med}) if $|S_{\mathrm{cpix}} - S_{\mathrm{med}}| > S_{\mathrm{med}} + 1$ mJy (van der Hulst et al. 1992). The 1-mJy offset prevents unnecessary filtering in noisy regions where the median is close to zero. Repeating the sensitivity measurements using the median-filtered version of the ATCA+Parkes map – where it was possible to measure the noise over much larger blank regions of sky – indicated rms values between 0.25 and 0.35 mJy per 40-arcsec beam, giving us confidence in our original sensitivity estimate for the data. The total flux density of the median-filtered map is 329 Jy, that is, the filtering operation removed ∼27 per cent of the total emission in the original 1.4-GHz map. Note that the filtering operation makes no distinction between background point sources and point sources that are intrinsic to the LMC, so this difference in flux density should not be interpreted as the contribution of background radio galaxies to the measured LMC flux density. We address the contribution from background galaxies in Section 4.2 below.

3.5 Total flux density of the LMC

For our final combined ATCA+Parkes map, we measure a total flux density of 443 Jy within a $10.^{\circ}8 \times 12.^{\circ}3$ field centred on $(05^{\mathrm{h}}20^{\mathrm{m}}, -68^{\mathrm{d}}44^{\mathrm{m}})_{\mathrm{J2000}}$. The total flux density in the Parkes map over this same region is 413 Jy. The difference in flux density between the

final merged map and the Parkes data is due to the relative calibration factor of 1.07 that we derived by comparing strong point sources in the Parkes and ATCA data sets. We note that the flux density of our Parkes 1.4-GHz map is ∼20 per cent less than the flux density quoted for the same map by Klein et al. (1989, 529 ± 29 Jy). This discrepancy can mostly be traced to the larger beam size that we have adopted for the Parkes data. Rather than the nominal half-power beamwidth (HPBW) of 15 arcmin, we determined an effective beam width of 16.55 arcmin by fitting point sources in the Parkes 1.4-GHz map with two-dimensional Gaussians. We believe that the effective beam width provides a more reliable estimate of the beam size of the Parkes data, since the gridding and scanning process used during observations and data reduction is known to slightly broaden the HPBW (e.g. Filipovic et al. 1995). Recalculating the total flux density in the Parkes map using the nominal beam size of 15.0 arcmin gives 503 Jy. We believe that the remaining discrepancy of ∼20 Jy between this value and the value determined by Klein et al. (1989) is due to methodological differences for measuring the LMC's integrated flux density. While we simply sum all the emission within the rectangular 10.°8 × 12.°3 map area, Klein et al. (1989) performed an integration in elliptical rings, including a correction for non-zero baselines. Towards the map edges, the Parkes data exhibit a small negative offset. By blanking pixels with negative values in the Parkes data and recalculating the integrated flux density over the remaining unmasked area, we find that the pixels at the map edges make an overall negative contribution of approximately −20 Jy to the measured flux density. For all further discussion in this paper, we confine our analysis to the central 7.°5 × 7.°5 region of our map, an area that comfortably encloses the LMC.

4 RESULTS

4.1 Radio continuum morphology

At 1.4 GHz, the radio continuum emission in the LMC is clearly dominated by the emission associated with the 30 Doradus region (see Figs 6 and 8). Across the LMC disc, there are numerous peaks of radio emission associated with individual H II regions and supernova remnants, but the distribution of the diffuse emission is quite asymmetric, showing a steep decline along the eastern edge of the LMC and a more gradual decrease with increasing distance from 30 Doradus in other directions. Fig. 7 presents north–south and east–west intensity profiles through 30 Doradus. As well as the abrupt eastern edge of the LMC's radio continuum emission, the profiles reveal that the intensity of the diffuse emission declines more slowly towards the south of 30 Doradus than to the north or the west. There is minimal diffuse emission along the western edge of the LMC, even surrounding active star forming complexes such as N11 and N87. We discuss a possible explanation for the asymmetric distribution of the diffuse radio emission in the LMC, and for the slower decline in emission's intensity south of 30 Doradus, in Section 4.6.

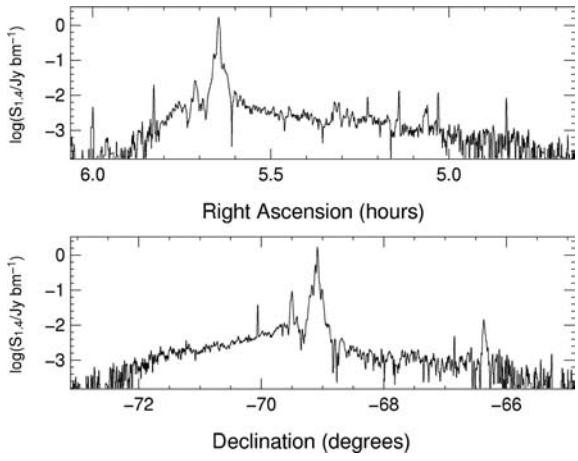

Figure 7. East–west (top panel) and north–south (bottom panel) intensity profiles through 30 Doradus. The profiles are shown with a logarithmic intensity scale to emphasize the behaviour of the diffuse emission.

4.2 Contribution from background point sources

Since the LMC subtends a large area on the sky, it is possible that background radio galaxies make a non-negligible contribution to the total 1.4-GHz flux density that we measure for the LMC. We have attempted to estimate this contribution using a direct and an indirect method. In the direct method, we used a smooth-and-mask technique to measure the point source flux in sixteen 1° × 1° control fields around the edges of our 1.4-GHz ATCA+Parkes map. We first convolved the ATCA+Parkes data with a 1 arcmin Gaussian kernel and masked all pixels in the four control fields where the flux density of the smoothed map was less than 0.8 mJy beam^{-1}. We measured the total flux density of the unmasked pixels in each of the control fields, and then calculated the mean flux density per square degree. Multiplying this by the area of the LMC yields an estimate of the flux density due to background sources. Assuming that the LMC has an angular size of 7.°5 × 7.°5, this method indicates that the 1.4-GHz flux density of sources behind the LMC is 46 ± 10 Jy, approximately 10 per cent of the LMC's measured total flux density.

We made a second, indirect estimate of the flux density due to background sources using the differential 1.4-GHz source count distributions of the FIRST and NVSS surveys determined by Blake & Wall (2002). We fitted a curve to the data presented in their fig. 5, and calculated the total flux density expected for sources in the flux density range [0.001, 1] Jy within an area of 7.°5 × 7.°5. The predicted 1.4-GHz flux density of background sources is 52 ± 3 Jy from the FIRST source count distribution and 55 ± 3 Jy from the NVSS data. These values are in reasonable agreement with our direct estimate from the ATCA+Parkes map, given the potential sources of uncertainty in our direct estimate.

4.3 Thermal fraction of radio emission at 1.4 GHz

Many of the brightest features in the 1.4-GHz radio map are also observed to be bright sources of Hα emission (see Fig. 8). This suggests that a significant fraction of the total 1.4-GHz radio continuum flux density may be produced by a few very bright star-forming regions, for example, 30 Doradus, N11 and N44. We used the Southern Hα Sky Survey Atlas (SHASSA) map of Hα emission in the LMC to obtain a rough estimate for the fraction of the LMC's 1.4-GHz flux density that is of thermal origin (Gaustad et al. 2001).[1] Our 1.4-GHz ATCA+Parkes map and the SHASSA map were regridded to a common pixel scale of 20 arcsec and a common 7.°5 × 7.°5 field of view. We measured the total flux density in the 1.4-GHz map for pixels with Hα emission above brightness thresholds of 100 and 500 R. The 1.4-GHz flux densities corresponding to these Hα brightness thresholds are 140 and 81 Jy, suggesting that the thermal fraction is of the LMC's 1.4-GHz radio continuum emission is likely to be greater than 20 per cent. Note that this estimate should be

[1] SHASSA is supported by the National Science Foundation.

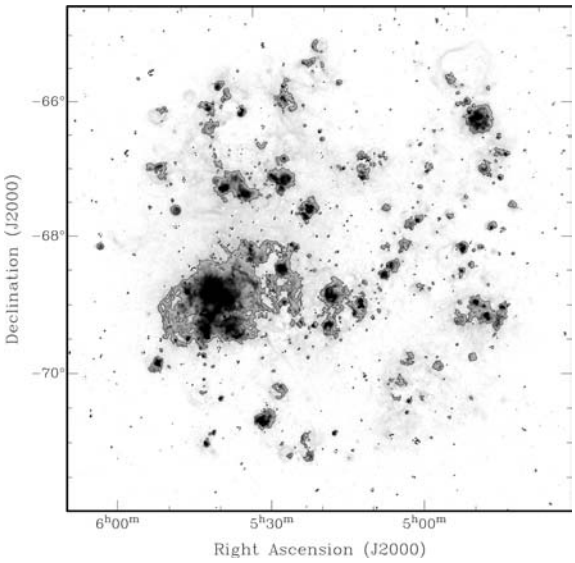

Figure 8. SHASSA map of Hα emission from the LMC (Gaustad et al. 2001). The black contours indicate an Hα brightness of 50 R. A square-root intensity scale has been used to emphasize the characteristics of the diffuse emission. Note that while the bright features in the Hα and 1.4-GHz radio continuum maps show good correspondence, the diffuse emission is brighter and more extended at radio wavelengths, particularly in the south–east of the LMC and in a central region around $(5^{\rm h}20^{\rm m}, -68^{\rm d}30^{\rm m})_{\rm J2000}$ (compare Fig. 6).

understood as providing only a general indication that the thermal fraction of the LMC's radio continuum emission is higher than for normal spiral galaxies, a phenomenon that appears to be relatively common amongst dwarf galaxies (e.g. Klein, Wielebinski & Thuan 1984). We have not accounted for extinction of the Hα emission, nor for the fact that most evolved H II regions will contain a mixture of non-thermal and thermal radio emission. We note that the flux density contained within a $0\overset{\circ}{.}5 \times 0\overset{\circ}{.}5$ box centred on 30 Doradus is 56 Jy, suggesting that 30 Doradus alone accounts for a significant fraction of the LMC's total and thermal radio flux density.

4.4 Star formation in the LMC

Since radio emission is unaffected by extinction, developing a reliable calibration for a galaxy's SFR based on its integrated radio flux density would be a valuable tool for studies of star formation at high redshift. However, the calibrations derived from local samples typically reflect the characteristic thermal/non-thermal emission ratio observed for normal galaxies (∼10 per cent, e.g. Condon 1992), and generally do not hold for young starbursts or dwarf galaxies (e.g. Roussel et al. 2003; Hunt, Bianchi & Maiolino 2005). Recently, Bell (2003) compared radio-derived SFRs to measurements determined from far-ultraviolet, infrared (IR) and optical data for a sample of 249 normal and irregular galaxies, and presented new radio and IR SFR calibrations that take account of the low-dust opacity and lower fraction of non-thermal radio emission in dwarf galaxies. We used equation (6) from Bell (2003) to estimate the LMC's SFR from its total radio continuum flux density, finding $\rm SFR_{RC} \sim 0.2\,M_\odot\,yr^{-1}$. This value agrees very well with the SFRs derived from the LMC's total infrared (TIR) and Hα luminosities. To estimate $\rm SFR_{TIR}$, we used the spectral energy distribution models presented in Dale & Helou (2002) to translate the Improved Reprocessing of the IRAS Survey (IRIS) 60- and 100-μm integrated fluxes of the LMC into an estimate of the TIR flux and equation (5) from Bell (2003) to calculate the $\rm SFR_{TIR}$, finding $\rm SFR_{TIR} \sim 0.2\,M_\odot\,yr^{-1}$.[2] The LMC's total H$\alpha$ luminosity, corrected for an average extinction of $A_V = 1$ across the LMC, is $4.1 \times 10^{41}\,\rm erg\,s^{-1}$ (Kennicutt & Hodge 1986). Applying the SFR calibration for Hα emission recently published by Calzetti et al. (2007) also results in $\rm SFR_{H\alpha} \sim 0.2\,M_\odot\,yr^{-1}$. While the SFRs derived using these three tracers are in excellent agreement, the supernova rate that they predict is $\sim$0.0016 $\rm yr^{-1}$, assuming a Salpeter initial mass function between 0.1 and 100 $\rm M_\odot$. If the LMC followed the standard relation observed for normal spiral galaxies (Condon 1992), this supernova rate should generate a non-thermal radio flux density of ∼530 Jy at 1.4 GHz, ∼20 per cent greater than the LMC's total observed 1.4-GHz flux density. It thus appears that while the LMC follows the radio-FIR correlation for normal galaxies (Hughes et al. 2006), it does not conform to the usual scaling relations between star formation and radio emission.

4.5 The radio spectral index

We used the Parkes map of the LMC at 4.8 GHz published by Haynes et al. (1991) in combination with our 1.4-GHz map to verify the LMC's total radio spectral index, and to investigate spatial variations of the radio spectral index within the LMC. We calculated the global spectral index using (i) the total flux densities measured over the commonly observed area at both frequencies, (ii) the total flux densities measured for a region where the 60 μm emission in the IRIS map of the LMC is greater than 0.9 MJy $\rm sr^{-1}$ (Miville-Deschênes & Lagache 2005) and (iii) the total flux densities measured over a smaller region where the 4.8-GHz emission was brighter than 40 mJy $\rm beam^{-1}$. The flux density of the LMC at 1.4 and 4.8 GHz within each of these three regions is listed in Table 2. The boundaries of each region are indicated on the map of the LMC in Fig. 9.

Our three estimates for the LMC's global radio spectral index are quite similar, ranging from $\alpha = -0.29$ for the measurement across the common $7\overset{\circ}{.}5 \times 7\overset{\circ}{.}5$ field, to $\alpha = -0.17$ for the more restricted region where the 4.8-GHz emission is brighter than 40 mJy $\rm beam^{-1}$. All three estimates are much flatter than the typical spectral index of normal spiral galaxies at these frequencies ($\alpha \sim -0.74 \pm 0.12$, Gioia, Gregorini & Klein 1982), suggesting that the thermal fraction of the LMC's radio continuum emission at 1.4 GHz is indeed relatively large. We note that our estimate is flatter than the spectral index between 20 MHz and 2.3 GHz determined for the LMC by Klein et al. (1989, $\alpha = -0.56 \pm 0.05$), but consistent with the spectral index at higher frequencies, $\alpha = -0.3 \pm 0.1$, indicated by the Haynes et al. (1991) data.

4.6 Spatial variation of the radial spectral index

To investigate spatial variations of the radio spectral index, we also produced a spectral index map. The map was constructed by smoothing the ATCA+Parkes 1.4-GHz image to the resolution of the Parkes data (4.8 arcmin), blanking pixels below a certain brightness threshold, and calculating the spectral index of the remaining high-signal-to-noise ratio (S/N) pixels. For both maps, we blanked pixels with a flux density less than 40 mJy $\rm beam^{-1}$ in the 4.8-GHz data; it was not necessary to perform additional masking based on the 1.4-GHz

[2] http://www.cita.utoronto.ca/∼mamd/IRIS/.

Table 2. The flux density, resolution and sensitivity of our original and median-filtered 1.4-GHz ATCA+Parkes maps and the 4.8-GHz map by Haynes et al. (1991). The second column lists the resolution (HPBW) of each image. The third column lists the flux density within the common $7\overset{\circ}{.}5 \times 7\overset{\circ}{.}5$ area surveyed at both frequencies (Region 1). The fourth column lists the flux density within the IRIS 60 μm 0.9 MJy sr^{-1} contour (Region 2, Miville-Deschênes & Lagache 2005). The fifth column lists the flux density within the 40 mJy beam^{-1} brightness threshold of the 4.8-GHz map, which defines the edges of our spectral index map (Region 3). The boundaries of these three regions are indicated in Fig. 9. The sixth column lists the sensitivity of each map, measured from blank regions of sky.

Frequency (GHz)	Beam (arcsec)	Flux density Region 1 (Jy)	Flux density Region 2 (Jy)	Flux density Region 3 (Jy)	Sensitivity
1.4	40	426	390	309	0.3 mJy per 40 arcsec beam
1.4-mf	40	367	350	277	0.3 mJy per 40 arcsec beam
4.8	288	296	291	250	9 mJy per 4.8 arcmin beam

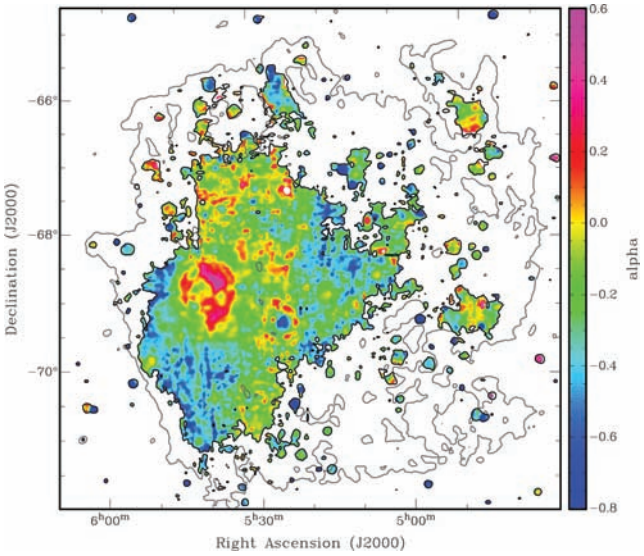

Figure 9. The spectral index map calculated from a smoothed version of the 1.4-GHz ATCA+Parkes map and the 4.8-GHz Parkes map of Haynes et al. (1991). The black line indicates the 40 mJy beam^{-1} brightness threshold of the 4.8-GHz map. The grey line reproduces the 0.9 MJy sr^{-1} contour of the IRIS 60 μm map of Miville-Deschênes & Lagache (2005), which approximately marks the boundary of the LMC's disc.

map since the 1.4-GHz data are more sensitive than the Parkes 4.8-GHz data. The resulting spectral index map is shown in Fig. 9. We note that our masking technique is biased against faint emission with a steep non-thermal spectral index, since pixels lacking high-S/N 4.8-GHz emission are excluded, even if 1.4-GHz emission at that position is well detected. The significance of this effect can be gauged by comparing our estimates of the global spectral index calculated over the three different fields of view. The common $7\overset{\circ}{.}5 \times 7\overset{\circ}{.}5$ field encloses approximately four times the number of unmasked pixels as our spectral index map, but the global radio spectral index determined for these two regions only varies by $\Delta\alpha \sim 0.1$. This suggests that the average spectral index in regions of the LMC excluded by the 40 mJy beam^{-1} brightness threshold in the 4.8-GHz map is only slightly steeper than for the regions that are included in our spectral index map.

The dominant feature of the spectral index map is the emission associated with 30 Doradus. The spectral index appears to become more negative with increasing distance from 30 Doradus, suggesting an increasing non-thermal fraction at larger radii. This transition is asymmetric, however: to the south–east of 30 Doradus, the spectral index decreases much more abruptly than in the north–west direction. Several of the LMC's well-known star-forming regions can also be identified in the spectral index map (e.g. N11, N87), and these exhibit a variegated pattern of positive and negative spectral indices. Overall, spectral indices across the LMC are relatively flat, and very few regions have spectral indices more negative than $\alpha \sim -0.7$. The most negative spectral indices, moreover, are associated with compact sources that are probably SNRs or background radio galaxies. A notable exception is an extended region of radio continuum emission with $\alpha \sim -0.4$ located at the interface of the LMC4 and LMC5 superbubbles, at an approximate position of $(05^{\rm h}25^{\rm m}, -66^{\rm d}15^{\rm m})_{\rm J2000}$. The H I, radio continuum and 8.3 μm emission from this region were studied in detail by Cohen et al. (2003), who identified the region as a site of triggered secondary star formation, containing a mixture of young massive stars and recently exploded supernova remnants.

In order to quantify the behaviour of the spectral index with increasing distance from 30 Doradus, we measured the average spectral index in circular annuli centred on $(05^{\rm h}38^{\rm m}42^{\rm s}, -69^{\rm d}06^{\rm m}03^{\rm s})_{\rm J2\,000}$. The width of each annulus was 7.2 arcmin to ensure that our measurements of the spectral index were statistically independent. We determined the average spectral index using two methods: (i) using the spectral index map shown in Fig. 9 directly and (ii) calculating the spectral index from the average 1.4- and 4.8-GHz flux density in each annulus. The average spectral indices determined by the two methods are in good agreement. A plot showing the behaviour of the spectral index as a function of distance from 30 Doradus is shown in Fig. 10.

The plots in Fig. 10 show that the radio spectral index departs from the average LMC value close to 30 Doradus. Within $R \sim 0.5$ kpc of 30 Doradus, the spectral index is more positive than the average value for the LMC, showing a pronounced bump that increases to positive values ($\alpha \sim 0.1$) at $R \sim 0.2$ kpc and then falls back to $\alpha \sim -0.2$ at $R \sim 0.5$ kpc. These positive spectral index values are visible in the spectral index map, particularly to the north–west of 30 Doradus. Clearly, a high fraction of the radio continuum emission close to 30 Doradus is of thermal origin, but it is not clear why the spectral index should increase and then decline over these spatial scales. Positive values of the radio spectral index can indicate regions where there is significant free–free absorption, which have been identified with extremely young ($\leqslant$1 Myr), dense, heavily embedded star clusters (e.g. Johnson & Kobulnicky 2003). However, these "ultradense H II regions" are typically very compact ($R \sim 2$ to 4 pc) and should be associated with extremely dense molecular gas (Elmegreen 2002): neither condition appears to be satisfied here. Based on a spectral analysis of OB stars in 30 Doradus, Walborn & Blades (1997) have suggested that the most recent star formation

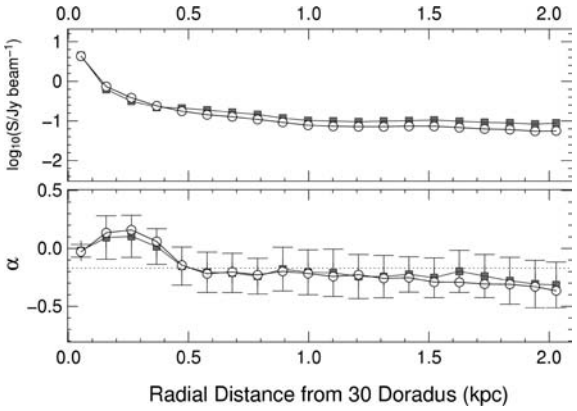

Figure 10. Variation in the radio flux density and spectral index, α, as a function of distance from 30 Doradus. The top panel shows the radial variation in the 1.4- (grey squares) and 4.8-GHz (open circles) flux density. The bottom panel shows the variation of the spectral index, as determined from the spectral index map (grey squares) and derived from the average 1.4- and 4.8-GHz flux density in each annulus (open circles). The error bars indicate the standard deviation of the pixel values in each annulus. The horizontal dotted line indicates the LMC's global spectral index that we measure, $\alpha = -0.23$.

activity in 30 Doradus is occurring to the north–west of the central R136 cluster, but their observations are again on much smaller spatial scales than those indicated here. At present, we have no good explanation for this feature. We note, however, that the feature is also present in a spectral index map constructed from Parkes data alone, which seems to rule out the possibility that it is an artefact of the ATCA 1.4-GHz data.

Beyond $R \sim 0.5$ kpc, the average spectral index exhibits a shallow decline with increasing distance from 30 Doradus, although the dispersion within each annulus is quite large. This steepening of the spectral index with increasing radius might indicate that the 30 Doradus region is the primary site of cosmic ray electron production in the LMC, and that synchrotron and inverse Compton losses are occurring as the relativistic electrons propagate away from the central star-forming region. Inspection of the spectral index map shows that this steepening of the spectral index is somewhat asymmetric: the spectral index remains relatively flat ($\alpha \sim -0.1$) to the north and west of 30 Doradus, but decreases more sharply towards the south and the east to values approaching $\alpha \sim -0.4$. The south-eastern region of the LMC is characterized by very high-H I column densities (e.g. Staveley-Smith et al. 2003), and radio continuum emission that is strongly polarized (e.g. Klein et al. 1993; Gaensler et al. 2005a). The NANTEN survey of ^{12}CO emission in the LMC shows that there is a long filament of molecular gas at this location, but the star-forming activity of this massive molecular cloud is relatively low (Fukui et al. 2001; Kawamura et al. 2005). A plausible physical scenario to explain both the relatively strong diffuse radio emission and the rapid steepening of the spectral index in this region would be an increased magnetic energy density. For a population of cosmic rays with relativistic energy spectrum $\mathrm{d}N/\mathrm{d}E \propto E^{-2}$, corresponding to a radio spectral index of $\alpha = -0.5$ at 1 GHz, the synchrotron emissivity scales as $B^{1.5}$. An amplified magnetic field, combined with the high gas densities and the intense radiation field surrounding 30 Doradus, would shorten the cooling time-scale of the electrons in this region, causing the radio spectral index to steepen. A stronger magnetic field is consistent with the unusually low-star-forming activity of the molecular clouds in this region, since higher magnetic pressures should also impede cloud collapse.

5 SUMMARY AND FINAL REMARKS

We present a sensitive ATCA+Parkes mosaic image of the 1.4-GHz radio continuum emission from the LMC that is suitable for studying emission on all scales greater than 40 arcsec. The reduction of this data involved a two-step deconvolution procedure that is able to recover both extended and point-like emission features, and a peeling technique that successfully removed calibration errors from bright off-axis sources. Our analysis of this data has shown:

(i) The diffuse radio continuum emission in the LMC has an asymmetric morphology, showing a steep decline along the eastern edge of the LMC and a more gradual decrease with increasing distance from 30 Doradus elsewhere. The intensity of the diffuse emission surrounding 30 Doradus remains stronger towards the south than in other directions, and is apparently correlated with the high-H I column densities in this region. A similar asymmetric morphology is seen in the 1.4–4.8 GHz spectral index map of the LMC. We suggest that a plausible explanation for these features is the amplification of the magnetic field in this region, perhaps due to field compression resulting from the motion of the LMC through the Milky Way's halo.

(ii) The total radio flux density of the LMC at 1.4 GHz is 426 Jy, of which $\geqslant$20 per cent probably has a thermal origin. The SFR implied by the LMC's total 1.4-GHz emission is $0.2\,\mathrm{M}_{\odot}\,\mathrm{yr}^{-1}$, in good agreement with SFRs derived from its IR and Hα luminosity (Bell 2003; Calzetti et al. 2007). This level of star formation significantly overpredicts the non-thermal flux density that should be generated by supernovae, however, suggesting that the LMC does not exhibit the same relationship between star formation and radio emission as normal spiral galaxies (e.g Condon 1992).

Finally, we note that these radio continuum data are available for use by the wider astronomical community. Our group is currently undertaking a study of the LMC's magnetic field, preparing a catalogue of 1.4 GHz point sources in the LMC, and comparing the LMC's 1.4-GHz radio continuum and FIR dust emission. However, the data should also be very useful for studies of individual objects such as supernova remnants, H II regions and planetary nebulae, and for detailed, galaxy-wide comparisons between the radio continuum emission and other tracers of star formation. The data may be retrieved from the website http://www.atnf.csiro.au/research/lmc_ctm/.

ACKNOWLEDGMENTS

AH would like to thank Tim Cornwell, Urvashi Rau and Enno Middelberg for useful discussions regarding peeling and synthesis imaging techniques. We also thank John Dickel, Marc-Antoine Miville-Deschênes and Guilaine Lagache for access to the Parkes 4.8 GHz, and IRIS 60 and 100 μm images that were used in this paper.

REFERENCES

Alves D. R., 2004, New Astron. Rev., 48, 659
Bell E. F., 2003, ApJ, 586, 794
Blake C., Wall J., 2002, MNRAS, 337, 993
Bressan A., Silva L., Granato G. L., 2002, A&A, 392, 377
Calzetti D. et al., 2007, ApJ, 666, 870
Cannon J. M., Skillman E. D., 2004, ApJ, 610, 772
Cohen M., Staveley-Smith L., Green A., 2003, MNRAS, 340, 275
Condon J. J., 1992, ARA&A, 30, 575
Dale D. A., Helou G., 2002, ApJ, 576, 159
Elmegreen B. G., 2002, ApJ, 577, 206

Filipovic M. D., Haynes R. F., White G. L., Jones P. A., Klein U., Wielebinski R., 1995, A&AS, 111, 311
Fukui Y., Mizuno N., Yamaguchi R., Mizuno A., Onishi T., 2001, PASJ, 53, L41
Gaensler B., Haverkorn M., Staveley-Smith L., Dickey J., McClure-Griffiths N., Dickel J., Wolleben M., 2005a, in Chyzy K. T., Otmianowska-Mazur K., Soida M., Dettmar R.-J., eds, The Magnetized Plasma in Galaxy Evolution, Jagiellonian University Press, Krakow, Poland, p. 209
Gaensler B. M., Haverkorn M., Staveley-Smith L., Dickey J. M., McClure-Griffiths N. M., Dickel J. R., Wolleben M., 2005b, Sci., 307, 1610
Gaustad J. E., McCullough P. R., Rosing W., Van Buren D., 2001, PASP, 113, 1326
Gioia I. M., Gregorini L., Klein U., 1982, A&A, 116, 164
Haynes R. F., Murray J. D., Klein U., Wielebinski R., 1986, A&A, 159, 22
Haynes R. F. et al., 1991, A&A, 252, 475
Helou G., Bicay M. D., 1993, ApJ, 415, 93
Hirashita H., Hunt L. K., 2006, A&A, 460, 67
Hughes A., Wong T., Ekers R., Staveley-Smith L., Filipovic M., Maddison S., Fukui Y., Mizuno N., 2006, MNRAS, 370, 363
Hunt L., Bianchi S., Maiolino R., 2005a, A&A, 434, 849
Johnson K. E., Kobulnicky H. A., 2003, ApJ, 597, 923
Kawamura A. et al., 2005, Protostars and Planets V, University of Arizona Press, Tucson, Arizona. p. 8300
Kennicutt R. C. Jr., 1998, ARA&A, 36, 189
Kennicutt R. C. Jr., Hodge P. W., 1986, ApJ, 306, 130
Kim S., Staveley-Smith L., Dopita M. A., Freeman K. C., Sault R. J., Kesteven M. J., McConnell D., 1998, ApJ, 503, 674
Kim S., Staveley-Smith L., Dopita M. A., Sault R. J., Freeman K. C., Lee Y., Chu Y., 2003, ApJS, 148, 473
Klein U., Wielebinski R., Thuan T. X., 1984, A&A, 141, 241
Klein U., Wielebinski R., Haynes R. F., Malin D. F., 1989, A&A, 211, 280
Klein U., Haynes R. F., Wielebinski R., Meinert D., 1993, A&A, 271, 402
Massey P., Lang C. C., Degioia-Eastwood K., Garmany C. D., 1995, ApJ, 438, 188
Meixner M. et al., 2006, AJ, 132, 2268
Miville-Deschênes M.-A., Lagache G., 2005, ApJS, 157, 302
Roussel H., Helou G., Beck R., Condon J. J., Bosma A., Matthews K., Jarrett T. H., 2003, ApJ, 593, 733
Sault R. J., Teuben P. J., Wright M. C. H., 1995, in ASP Conf. Ser. 77, Astronomical Data Analysis Software and Systems IV. Astron. Soc. Pac., San Francisco, p. 433
Sault R. J., Staveley-Smith L., Brouw W. N., 1996, A&AS, 120, 375
Smith R. C., MCELS Team, 1998, PASA, 15, 163
Stanimirovic S., 2002, in Stanimirovic S., Altschuler D., Goldsmith P., Salter C., eds, Astronomical Society of the Pacific Conference Series. Vol. 278, Single-Dish Radio Astronomy: Techniques and Applications. Astron. Soc. Pac., San Francisco, p. 375
Staveley-Smith L., Kim S., Calabretta M. R., Haynes R. F., Kesteven M. J., 2003, MNRAS, 339, 87
Steer D. G., Dewdney P. E., Ito M. R., 1984, A&A, 137, 159
van der Hulst J. M., Terlouw J. P., Begeman K. G., Zwitser W., Roelfsema P. R., 1992, in ASP Conf. Ser. 25, Astronomical Data Analysis Software and Systems I. Astron. Soc. Pac., San Francisco, p. 131
van der Marel R. P., Cioni M.-R. L., 2001, AJ, 122, 1807
Walborn N. R., Blades J. C., 1997, ApJS, 112, 457

This paper has been typeset from a TEX/LATEX file prepared by the author.